INTERNATIONAL JOURNAL FOR NUMERICAL METHODS IN FLUIDS
Int. J. Numer. Meth. Fluids 2000; **32**: 369–406

Large eddy simulation of subsonic and supersonic channel flow at moderate Reynolds number

E. Lenormand[a], P. Sagaut[b,*] and L. Ta Phuoc[b]

[a] *ONERA, DSNA/ETRI, 29 av. de la Division Leclerc, 92322 Châtillon cedex, France*
[b] *ONERA and LIMSI, CNRS, BP 133, 91403 Orsay, France*

SUMMARY

Large eddy simulation (LES) of compressible periodic channel flow is performed using a fourth-order finite difference scheme for a Reynolds number based on bulk density, bulk velocity and channel half-width equal to 3000. Two configurations are studied: a subsonic case ($M_0 = 0.5$) that corresponds to the experiments of Niederschulte *et al.* ['Measurements of turbulent flow in a channel at low Reynolds numbers', *Exp. Fluids*, **9**, 222–230 (1990)] and a supersonic case ($M_0 = 1.5$) that corresponds to the direct numerical simulation (DNS) results by Coleman *et al.* ['A numerical study of turbulent supersonic isothermal-wall channel flow', *J. Fluid Mech.*, **305**, 159–183 (1995); 'Compressible turbulent channel flows: DNS results and modeling', *J. Fluid Mech.*, **305**, 185–218 (1995)]. In order to determine the influence of the discretization, two cases are computed using two different meshes, a coarse one and a fine one. Two subgrid-scale models are tested: the first one is an extension to compressible flows of the Smagorinsky model, while the second one is a model based both on large and small scales of turbulence, a hybrid Bardina–selective mixed scale model. Various statistical comparisons are made with experimental and DNS data at similar Reynolds numbers, including higher-order statistics. Copyright © 2000 John Wiley & Sons, Ltd.

KEY WORDS: large eddy simulation; compressible flow; channel flow; subgrid-scale model

1. INTRODUCTION

Currently, the large eddy simulation (LES) method is more and more used for the unsteady calculation of turbulent flows. In LES, one computes the dynamics of the large, energy containing structures, while modelling the effect of smaller scales, referred to as the subgrid-scales (SGS), on the resolved ones through the use of a subgrid model. Thus, one of the main uncertainties of the LES technique lies in its SGS parameterization. SGS models that faithfully predict the dynamics of that interaction between resolved and unresolved scales have to be developed and validated.

* Correspondence to: ONERA, DSNA/ETRI, 29 av. de la Division Leclerc, 92322 Châtillon cedex, France. Tel: + 33 1 46734271; fax: + 33 1 46734146; e-mail: sagaut@onera.fr

CCC 0271–2091/2000/040369–38$17.50

Received 15 January 1998
Revised 16 February 1999

Most of the existing SGS models are based on the statistical description of the dynamics of the incompressible isotropic turbulence, and give satisfactory results when applied to that category of flows (see [1–3] for a comprehensive review). However, it is well known that SGS models must be modified to get reliable results when they are applied to flows whose dynamics differ greatly from those of isotropic turbulence. This is especially the case of wall-bounded flows: most of the existing models seem to be unable to account for the turbulence producing events that take place in the buffer zone of the boundary layer [4]. In order to maintain the reliability of the simulation, the computational grid is refined in such a way that these events are directly captured by the simulation, and the models are expected to vanish in this region.

Another issue concerning the SGS modelling is the compressibility effect. Basic SGS modelling is derived in the incompressible case, and one has to deal with additional physical mechanisms, at least when considering the energy equation. The problem of designing SGS models for compressible flows has only recently been addressed by some authors [5–7], but only few results have been reported in comparison with the incompressible case. Most of the existing LES of compressible flows are related to homogeneous flows [6,43] or free shear layer [8]. Some LES of compressible inhomogeneous flows have nevertheless been carried out [5].

This paper addresses the LES of compressible wall-bounded turbulence, both in the subsonic and supersonic regime. It is often assumed that only the compressibility effects associated with the variations of the mean quantities are significant, those associated with turbulent fluctuation being negligible. Recent direct numerical simulations (DNS) by Coleman *et al.* [9] in the supersonic regime have demonstrated this point, and pointed out that the Morkovin hypothesis remains valid at a Mach number equal to 3, but that the strong Reynolds analogy needs to be revisited in the cold-wall case. The main goal of this work is to assess the capability of LES to handle these flows.

The selected configuration is the isothermal-wall plane channel flow, because most of the wall turbulence interactions are represented in it, while it is very simple from a geometrical point of view. Two cases are considered, corresponding to the subsonic ($M_0 = 0.5$) and supersonic ($M_0 = 1.5$) regimes. Because sharp gradients of density and temperature in the near-wall region are known to affect the turbulence, the cold-wall case is considered here.

In the incompressible case, since the pioneering works of Deardorff [10] and Schumann [11], a large number of LES of that flow have been performed, the first reliable results including wall resolution being obtained by Moin and Kim [12]. High Reynolds number simulation ($Re \approx 1000$), including wall resolution, have recently been carried out [14]. Only few realizations are known in the compressible case. Ridder and Beddini [15] have carried out simulations in the low subsonic ($M = 0.3$) and the high subsonic ($M = 0.7$) cases, using an extension of the anisotropic SGS model of Schumann [11]. Wang and Pletcher [16] perfomed LES of a low-speed flow with significant heat transfer at the wall, using a low-Mach number algorithm coupled to a dynamic eddy viscosity model.

Another important issue concerning LES is the control of the numerical error. Theoretical works [17] and numerical experiments [13] both demonstrate the strong influence of numerical errors on the results. The use of a centred second-order-accurate scheme yields large errors in the incompressible case in the near-wall region. The skew-symmetric form of the convection term seems to be optimal in the incompressible case for the velocity–pressure formulation of the Navier–Stokes equations with regard to the aliasing the error. As for the modelling topic,

few results are known about these points in the compressible case but several authors have used that form for shock-free problems [6,18].

The paper is organized as follow: Section 2 describes the governing equations and the filtering operation, Section 3 sets out the numerical method and Section 4 is devoted to the SGS models. Section 5 presents the results for both the subsonic and the supersonic cases. Finally, a conclusion is drawn in Section 6.

2. GOVERNING EQUATIONS

2.1. Basic equations

The selected mathematical model for the description of the flow is the set of the Navier–Stokes equations representing the conservation of mass, momentum and energy. Written in conservative form for the conservative variables (density ρ, momentum ρu_i and total energy E) and using the summation convention for the repeated indices, they read

$$\frac{\partial \rho}{\partial t} + \frac{\partial}{\partial x_j}(\rho u_j) = 0, \tag{1}$$

$$\frac{\partial}{\partial t}(\rho u_i) + \frac{\partial}{\partial x_j}(\rho u_i u_j) + \frac{\partial p}{\partial x_i} + f_i \delta_{i1} = \frac{\partial \sigma_{ij}}{\partial x_j}, \tag{2}$$

$$\frac{\partial E}{\partial t} + \frac{\partial}{\partial x_j}(E+p)u_j + f_1 u_1 = \frac{\partial}{\partial x_j}\sigma_{ij} u_i - \frac{\partial}{\partial x_j} q_j, \tag{3}$$

where t and x_i are the independent variables representing time and spatial co-ordinates respectively, and $f_i \delta_{i1}$ is a volume force in the streamwise direction. The density ρ, the pressure p and the temperature T are linked by the state law for perfect gas,

$$\frac{p}{\rho} = \frac{T}{\gamma M_0^2}. \tag{4}$$

The total energy E is given by the relation

$$E = \frac{p}{\gamma - 1} + \frac{1}{2}\rho\, u_j u_j, \tag{5}$$

and the viscous stress tensor σ_{ij} depends on both the temperature T and the velocity u

$$\sigma_{ij} = \frac{\mu(T)}{Re} S_{ij}, \tag{6}$$

where the dimensionless viscosity μ is the quotient of the physical viscosity μ_p by the physical wall viscosity μ_0,

$$\mu(T) = \frac{\mu_p}{\mu_0}, \tag{7}$$

and the shear stress tensor $S = S(u)$ is given as

$$S_{ij} = S_{ij}(u) = \frac{\partial u_i}{\partial x_j} + \frac{\partial u_j}{\partial x_i} - \frac{2}{3}\delta_{ij}\frac{\partial u_k}{\partial x_k}. \tag{8}$$

The tensor δ_{ij} is the Kronecker symbol defined as $\delta_{ij} = 1$ if $i = j$ and $\delta_{ij} = 0$ otherwise. In addition, the heat flux is given by

$$q_j = \frac{-\mu}{(\gamma - 1)RePrM_0^2}\frac{\partial T}{\partial x_j}. \tag{9}$$

The equations have been made dimensionless by introducing reference length, velocity, density temperature and viscosity. Non-dimensional parameters are the Mach number, M_0, based on the bulk velocity U_b and wall sound speed. The Reynolds number, Re, is based on bulk density, bulk velocity, channel half-width, δ_h, and wall viscosity. The Prandtl number, Pr, and the ratio of specific heat are set equal to a constant 1.4 (the admitted value for the air).

The fluid is assumed to be an ideal gas with a power law temperature-dependent viscosity [19],

$$\mu(T) \cong T^{0.7}. \tag{10}$$

In order to keep the computational cost moderate, the simulation is of temporal type, i.e. periodic boundary conditions are used in the streamwise and spanwise directions. Thus, to preserve streamwise homogeneity, the flow must be driven by a uniform (in space) body force, f_i, which is non-zero only for $i = 1$ and is chosen to vary in time such that the total mass flux remains constant,

$$\frac{\partial}{\partial t}\int_0^2 \langle \rho u_1 \rangle \, \mathrm{d}z = 0, \tag{11}$$

where the brackets denote averaging over homogeneous planes parallel to the walls, which are located $z = 0$ and $z = 2$.

2.2. Filtered equations

Governing equations of LES are obtained through the application of a filter to the Navier–Stokes equations. Any flow variable ϕ can be written as $\phi = \bar{\phi} + \phi'$, where $\bar{\phi}$ represents the low frequency (or large-scale) part of the variable and ϕ' its high frequency (or small-scale)

part. The filtering operator is classically defined as a convolution operator on the computational domain Ω,

$$\bar{\phi} = \int_{\Omega} G_{\Delta}(\vec{x} - \vec{\xi})\phi(\vec{\xi})\, \mathrm{d}\vec{\xi}, \tag{12}$$

where G_{Δ} is the kernel filter function satisfying the normalization relation

$$\int_{\Omega} G_{\Delta}\, \mathrm{d}\vec{\xi} = 1, \tag{13}$$

and Δ is the cut-off length-scale associated with the filter.

The filtering operator is assumed to commute with time and spatial derivatives so that the continuity equation for the filtered field holds.

For compressible flows, it is convenient to introduce a related, density-weighted, filtering operator given by Favre [20] as

$$\tilde{\phi} = \frac{\overline{\rho\phi}}{\bar{\rho}}. \tag{14}$$

Now, any flow variable is decomposed as $\phi = \tilde{\phi} + \phi''$ and it is important to notice that the double prime now represents a mass-weighted SGS fluctuation. This mass-weighted averaging procedure reduces the inertia-related terms of the resolved density and internal energy equations to a form very similar to the incompressible case.

The application of the aforementioned definitions to the continuity and momentum equations is straightforward, yielding the following dimensionless filtered equations:

$$\frac{\partial \bar{\rho}}{\partial t} + \frac{\partial \bar{\rho}\tilde{u}_j}{\partial x_j} = 0, \tag{15}$$

$$\frac{\partial \bar{\rho}\tilde{u}_i}{\partial t} + \frac{\partial}{\partial x_j}\bar{\rho}\tilde{u}_i\tilde{u}_j + \frac{\partial \bar{p}}{\partial x_i} - \frac{\partial \hat{\sigma}_{ij}}{\partial x_j} + f_1 = -\frac{\partial}{\partial x_j}\tau_{ij} + \frac{\partial}{\partial x_j}(\overline{\sigma_{ij}} - \hat{\sigma}_{ij}), \tag{16}$$

where τ_{ij} and $\hat{\sigma}_{ij}$ are given respectively by

$$\tau_{ij} = -\bar{\rho}(\widetilde{u_i u_j} - \tilde{u}_i\tilde{u}_j), \tag{17}$$

$$\hat{\sigma}_{ij} = \frac{\mu(\tilde{T})}{Re}\left(\frac{\partial \tilde{u}_i}{\partial x_j} + \frac{\partial \tilde{u}_j}{\partial x_i} - \frac{2}{3}\delta_{ij}\frac{\partial \tilde{u}_k}{\partial x_k}\right). \tag{18}$$

Filtering the energy conservation equation is a more problematic task because it can be performed in several ways depending on the initial formulation of the equation, and also on the set of chosen basic variables. For example, filtering an equation written in terms of pressure/temperature does not lead to the same SGS terms as filtering an equation written in

terms of enthalpy/temperature. In this work, a modified energy $\hat{E}$ is introduced following Vreman [7,8,21] such that its definition is the same as Equation (5) but written in terms of filtered variables

$$\hat{E} = \frac{\bar{p}}{\gamma - 1} + \frac{1}{2}\bar{\rho}\tilde{u}_j\tilde{u}_j. \tag{19}$$

One can show that this modified energy follows the evolution equation:

$$\frac{\partial \hat{E}}{\partial t} = \frac{1}{(\gamma - 1)}\frac{\partial \bar{p}}{\partial t} + \tilde{u}_i\frac{\partial \bar{\rho}\tilde{u}_i}{\partial t} + \frac{1}{2}\tilde{u}_i\tilde{u}_j\frac{\partial \bar{\rho}\tilde{u}_j}{\partial x_j}. \tag{20}$$

Using this definition and after some calculations one derives the filtered energy conservation equation:

$$\frac{\partial \hat{E}}{\partial t} + \frac{\partial}{\partial x_j}((\hat{E} + \bar{p})\tilde{u}_j) - \frac{\partial}{\partial x_j}(\hat{\sigma}_{ij}\tilde{u}_i) + \frac{\partial \hat{q}_j}{\partial x_j} + f_1\tilde{u}_1 = -B_1 - B_2 - B_3 + B_4 + B_5 + B_6 - B_7, \tag{21}$$

where the filtered heat flux can be expressed as a function of the filtered variables

$$\hat{q}_j = \frac{-\mu(\tilde{T})}{(\gamma - 1)RePrM_0^2}\frac{\partial \tilde{T}}{\partial x_j}. \tag{22}$$

It is noticed that the left-hand sides of Equations (15), (16) and (21) have the same form as that of the non-filtered equations (1)–(3), except that the argument is now about the filtered variables.

The right-hand sides of Equations (16) and (21) are the SGS terms that must be parameterized, i.e. expressed as function of the basic filtered variables $\bar{\rho}$, $\tilde{u}_i$, and $\bar{p}$.

The subgrid terms $B_1 \ldots B_7$ in the energy equation are defined as

$$B_1 = \frac{1}{\gamma - 1}\frac{\partial}{\partial x_j}(\overline{pu_j} - \bar{p}\tilde{u}_j), \tag{23}$$

$$B_2 = \overline{p\frac{\partial u_k}{\partial x_k}} - \bar{p}\frac{\partial \tilde{u}_k}{\partial x_k}, \tag{24}$$

$$B_3 = \frac{\partial}{\partial x_j}(\tau_{kj}\tilde{u}_k), \tag{25}$$

$$B_4 = \tau_{kj}\frac{\partial}{\partial x_j}\tilde{u}_k, \tag{26}$$

$$B_5 = \overline{\sigma_{kj}\frac{\partial}{\partial x_j}u_k} - \overline{\sigma_{kj}}\frac{\partial}{\partial x_j}\tilde{u}_k, \tag{27}$$

$$B_6 = \frac{\partial}{\partial x_j}(\overline{\sigma_{ij}}\tilde{u}_i - \widehat{\sigma_{ij}}\tilde{u}_i), \tag{28}$$

$$B_7 = \frac{\partial}{\partial x_j}(\overline{q_j} - \widehat{q_j}). \tag{29}$$

It is very important to notice that this formulation is free of any hypothesis on the incompressibility of the small turbulent scales [6]. Thus, at that stage, absolutely no term has been neglected. The set of filtered Navier–Stokes equations is completed by the filtered state law,

$$\bar{p} = \frac{\bar{\rho}\tilde{T}}{\gamma M^2}, \tag{30}$$

which expresses the filtered temperature as a function of filtered pressure and density.

3. NUMERICAL METHOD

This section details the numerical algorithm used to solve the filtered Navier–Stokes equations.

3.1. Time integration

The time integration is performed using an explicit low-storage third-order Runge–Kutta (RK3) scheme. Consider the following conservation equation for an arbitrary variable W

$$\frac{\partial W}{\partial t} + H(W) = 0. \tag{31}$$

The RK3 scheme reads

$$\begin{aligned} &W_1 = W^n + \gamma_1 \cdot \Delta t \cdot H(W^n), \quad H_1 = H(W_1) + \chi_1 H(W_0), \\ &W_2 = W_1 + \gamma_2 \cdot \gamma_2 \cdot \Delta t \cdot H_1, \quad H_2 = H(W_2) + \chi_2 H_1, \\ &W^{n+1} = W_2 + \gamma_3 \cdot \Delta t \cdot H_2, \end{aligned} \tag{32}$$

where Δt is the time step and γ_1, γ_2, γ_3, χ_1 and χ_2 are constants proposed by Lowery and Reynolds [22].

The moderate Courant–Friedrich–Lewy (CFL) number that can be reach using this scheme ensures that the time step will remain small, and that the time filtering due to the use of finite time steps will be masked by the space-filtering operation.

3.2. Space discretization

A fourth-order-accurate centred finite difference scheme is used for the convective and pressure gradient terms

$$\left.\frac{\partial U}{\partial x}\right|_i = \frac{U_{i-2} - 8U_{i-1} + 8U_{i+1} - U_{i+2}}{12\Delta x} + O(\Delta x^4). \tag{33}$$

In the wall-normal direction, a Cartesian non-uniform grid is employed and a mapping is used to compute the derivatives on a regular η space,

$$\frac{\partial u}{\partial z} = \frac{\partial u}{\partial \eta}\frac{\partial \eta}{\partial z}, \tag{34}$$

where the Jacobian term $\partial\eta/\partial z$ is computed with the fourth-order-accurate aforementioned scheme using the relation

$$\frac{\partial \eta}{\partial z} = \left(\frac{\partial z}{\partial \eta}\right)^{-1}. \tag{35}$$

Another important point is that the aliasing error must be as small as possible in order to allow the method to be stable. Following the conclusions of Kravchenko and Moin [13], the convective terms in the Navier–Stokes equations are discretized in the skew-symmetric form as

$$\frac{\partial}{\partial x_j}(\tilde{u}_j\psi) = \frac{1}{2}\left(\frac{\partial}{\partial x_j}(\tilde{u}_j\psi) + \tilde{u}_j\frac{\partial \psi}{\partial x_j} + \psi\frac{\partial \tilde{u}_j}{\partial x_j}\right), \tag{36}$$

where ψ is an arbitrary convected field.

Diffusive terms and SGS terms are discretized with a second-order centred scheme. In the streamwise and spanwise directions, the scheme reads

$$\left.\frac{\partial U}{\partial x}\right|_i = \frac{U_{i+1} - U_{i-1}}{2\Delta x} + O(\Delta x^2), \tag{37}$$

while in the wall-normal direction, the scheme reads

$$\left.\frac{\partial U}{\partial z}\right|_k = \frac{1}{(\Delta z_{k-1} + \Delta z_k)}\left(\frac{\Delta z_{k-1}}{\Delta z_k}(U_{k+1} - U_k) + \frac{\Delta z_k}{\Delta z_{k-1}}(U_k - U_{k-1})\right) + O(\Delta z^2), \tag{38}$$

with $\Delta z_k = z_{k+1} - z_k$.

An adaptative time stepping procedure based on a linear stability analysis is implemented in order to enhance the computational efficiency. The chosen CFL number is 0.95 but some calculations have shown that the numerical method is stable for CFL numbers as large as 1.5.

3.3. Forcing term

As pointed out in the previous section, because the flow is periodic in the streamwise direction, it must be driven by a uniform body force f_1 to preserve homogeneity. Averaging the momentum equation (16) over xy planes and integrating the result in the wall-normal direction, one obtains

$$\frac{\partial}{\partial t} Q_{\mathrm{m}} = \frac{1}{Re} L_y \left[\langle \mu \rangle \frac{\partial \langle u_1 \rangle}{\partial z} \right]_{\mathrm{low}}^{\mathrm{up}} - L_y L_z f_1, \tag{39}$$

where the $\langle\ \rangle$ operator stands for averaging over the xy plane, L_z is the width of the channel, L_y its span and Q_{m} is the mean flux of the flow across a yz section. The subscript and superscript low and up stand for the lower and upper wall respectively.

As long as

$$\langle \mu \rangle \frac{\partial \langle u_1 \rangle}{\partial z}\bigg|_{\mathrm{up}} = -\langle \mu \rangle \frac{\partial \langle u_1 \rangle}{\partial z}\bigg|_{\mathrm{low}},$$

one gets

$$\frac{\partial Q_{\mathrm{m}}}{\partial t} = -L_y L_z f_1 - \frac{2L_y}{Re} \langle \mu \rangle \frac{\partial \langle u_1 \rangle}{\partial z}\bigg|_{\mathrm{low}}. \tag{40}$$

This equation shows that if a constant forcing term f_1 is imposed, while the flow undergoes a transition leading to an increase of the shear stress

$$\langle \mu \rangle \frac{\partial \langle u_1 \rangle}{\partial z}\bigg|_{\mathrm{low}},$$

the mass flux will decrease. So, if a constant mass flux ($\partial Q_{\mathrm{m}}/\partial t = 0$) is desired, the driving term f_1 must be time-dependent. Rather than crudely using Equation (40), which could lead to numerical instability, an extension to compressible flows of the algorithm proposed by Deschamps [23] is used to compute the driving term at each time step.

Supposing that the driving term f_1^n at time step n is known then f_1^{n+1} is computed using the relation

$$f_1^{n+1} = f_1^n + \frac{\Delta t}{L_y L_z} [\alpha(Q^{n+1} - Q_0) + \beta(Q^n - Q_0)], \tag{41}$$

where Q_0, Q^n and Q^{n+1} are, respectively, the mass flux (supposed to be conserved), the mass flux at time step n and a first-order predictor of the mass flux at time step $n+1$, given by

$$Q^{n+1} = Q^n - \Delta t g^n, \tag{42}$$

with

$$g^n = L_y L_z f^n + \frac{2L_y}{Re} \langle \mu^n \rangle \left. \frac{\partial \langle u_1^n \rangle}{\partial z} \right|_{\text{low}}. \tag{43}$$

A stability analysis shows that the algorithm is most efficient for $\alpha = 2/\Delta t$ and $\beta = -0.2/\Delta t$.

To be consistent with the momentum equation, a driving term $f_1 u_1$ must be added to the energy equation. Experiments show that the computation is stable only if one substitutes $f_1 u_1$ with $f_1 u_{1b}$, where u_{1b} is the bulk velocity of the flow

$$u_{1b} = \frac{Q_m}{\dfrac{1}{L_z} \displaystyle\int_0^2 \langle \rho \rangle \, dz}. \tag{44}$$

This algorithm has proven to be very efficient as long as the mass flux is conserved within 0.01% in the long-term integration.

3.4. Boundary conditions

Isothermal no-slip boundary conditions are imposed at the walls:

$$T = T_w, \qquad u_k = 0, \quad k = 1, 2, 3, \tag{45}$$

where the wall temperature T_w is chosen as a reference and is then taken equal to 1. Furthermore, the pressure at a wall is computed writing the wall-normal momentum equation at this location

$$\frac{\partial p}{\partial z} = -\frac{\partial}{\partial z}(\bar{\rho} \widetilde{u_3}^2) + \frac{4}{3Re} \frac{\partial}{\partial z} \left(\bar{\mu} \frac{\partial \widetilde{u_3}}{\partial z} \right) + \frac{1}{Re} \frac{\partial}{\partial x} \mu \frac{\partial \widetilde{u_1}}{\partial z} + \frac{1}{Re} \frac{\partial}{\partial y} \mu \frac{\partial \widetilde{u_2}}{\partial z}. \tag{46}$$

The equation is discretized using the aforementioned schemes in the streamwise and spanwise directions and using a non-centred second-order-accurate scheme in the wall-normal direction. For example, for the lower wall, it reads

$$\left. \frac{\partial U}{\partial z} \right|_{\text{low}} = \frac{4U_2 - U_3}{2\Delta_1}, \tag{47}$$

where $\Delta_1 = z_2 - z_1$. Thus, one can compute the pressure at a wall. Computing the density is straightforward using the state law (30), and the total energy is given as

$$E|_{\text{wall}} = \frac{p|_{\text{wall}}}{(\gamma - 1)}. \tag{48}$$

As already said in previous sections, periodic boundary conditions are used in the streamwise and spanwise directions,

$$\phi(x, . , .) = \phi(x + L_x, . , .), \qquad \phi(. , y, .) = \phi(. , y + L_y, .), \tag{49}$$

where ϕ is any conservative variable.

3.5. Initial conditions

Initial conditions for the computations were defined by superimposing a random velocity fluctuation whose amplitude is 10% of the mean velocity upon a laminar parabolic Poiseuille velocity profile,

$$U_1(t = 0) = U_{1\max}(1 - (z - 1)^2)(1 + \epsilon), \tag{50}$$

$$U_2(t = 0) = 0, \tag{51}$$

$$U_3(t = 0) = 0. \tag{52}$$

The perturbation function ϵ is given as $\epsilon = 0.1g$, where g is a random variable ranging from -1 to $+1$. The maximum velocity $U_{1\max}$ at the centre of the channel is set to 1.5.

A uniform density field is imposed while the temperature profile is calculated using the laminar distribution [24]

$$T(t = 0) = 1 + \frac{(\gamma - 1)PrM_0^2}{3} U_{1\max}(1 - (z - 1)^4). \tag{53}$$

4. SUBGRID-SCALE MODEL

As already seen in Section 2.2, the effects of unresolved scales of motion on large scales appear through SGS terms in the right-hand-sides of Equations (16) and (21).

The main features of the SGS model for both the momentum and energy equations used for the calculations are detailed in this section.

4.1. Momentum equation

The SGS term $\partial/\partial x_j(\overline{\sigma_{ij}} - \widehat{\sigma_{ij}})$ has been neglected in the momentum equation following the *a priori* evaluation of Vreman *et al.* [7,25], who found for a mixing layer case in which the Mach number is lower than 1.2

$$O\left(\frac{\partial}{\partial x_j}(\overline{\sigma_{ij}} - \widehat{\sigma_{ij}})\right) \approx \frac{1}{100} O\left(\frac{\partial}{\partial x_j}\tau_{ij}\right). \tag{54}$$

This result is assumed to be valid in the present cases.

4.1.1. Smagorinsky model. The deviatoric part of the SGS stress tensor τ_{ij} is parameterized via an eddy viscosity model, based on the Boussinesq hypothesis using an extension of the classical Smagorinsky model,

$$\tau_{ij} - \frac{1}{3}\tau_{kk}\delta_{ij} = \tau_{ij}^{D} = -\bar{\rho} v_t S_{ij}(\tilde{u}). \tag{55}$$

The eddy viscosity v_t is derived from a Prandtl-like mixing length assumption. It is assumed to be proportional to a characteristic length scale Δ and to a characteristic time scale based on the second invariant of the filtered shear stress tensor $S(\tilde{u})$,

$$v_t = (C_s\Delta)^2 |S(\tilde{u})|, \tag{56}$$

with

$$|S(\tilde{u})|^2 = \frac{1}{2} S_{ij}(\tilde{u}) S_{ij}(\tilde{u}). \tag{57}$$

The theoretical value of the parameter C_s is found to be equal to 0.18 for incompressible homogeneous isotropic turbulence. Nevertheless, this parameter is widely dependent on the flow and Deardorff [10] proposed to reduce its value to 0.1 when considering the plane channel flow.

The characteristic length scale is usually chosen to be

$$\Delta = (\Delta x \Delta y \Delta z)^{1/3}, \tag{58}$$

where Δx, Δy and Δz are mesh sizes in the x-, y- and z-directions respectively.

The main drawbacks of this model come from the fact that it depends exclusively on large scales, so it does not vanish, neither in the vicinity of a solid wall, nor in the laminar shear flows. Furthermore, this model is known to be too dissipative in transitional flows so that transition can be delayed or inhibited.

In order to enforce the model to vanish in the near-wall region, the mixing length $C_s\Delta$ is corrected using the Van Driest damping function

$$1 - \mathrm{e}^{z^+/a}, \tag{59}$$

where a is a constant taken to be approximately 25 and z^+ is the distance from the wall expressed in wall units.

4.1.2. The mixed scale model. Difficulties mentioned above can be alleviated by developing models depending on both large and small scales. Such models have been proposed by Sagaut [3] and Ta Phuoc [26]. These mixed scale models form a one-parameter (α) family of SGS models. The eddy viscosity is given using a non-linear combination of the second invariant of the shear stress tensor, the characteristic length scale Δ and the small-scale kinetic energy q_c^2,

$$\nu_t = C_m |S|^{\alpha} (q_c^2)^{(1-\alpha)/2} \Delta^{(1+\alpha)}, \tag{60}$$

where $|S|$ is computed using Equation (57) and the test field kinetic energy q_c^2 is evaluated as

$$q_c^2 = \frac{1}{2} (\tilde{u}_i)'(\tilde{u}_i)'. \tag{61}$$

The test field $(\tilde{u}_i)'$ is extracted from the resolved field employing a test filter denoted by a widehat

$$(\widetilde{u}_i)' = \widetilde{u}_i - \widehat{\widetilde{u}_i}. \tag{62}$$

Because of the realizability conditions imposed on the SGS term, τ_{ij} [7]

$$\tau_{ii} \geq 0, \tag{63}$$

$$|\tau_{ij}| \leq (\tau_{ii}\tau_{jj})^{1/2}, \tag{64}$$

$$\det(\tau_{ij}) \geq 0. \tag{65}$$

The test filter must be positive, i.e. the kernel filter function defined in Equation (12) must fulfil the condition

$$G_{\Delta} \geq 0. \tag{66}$$

The test filter presently used is a local weighted-average

$$\widehat{\widetilde{u}_i} = \frac{1}{4}\tilde{u}_{i-1} + \frac{1}{2}\tilde{u}_i + \frac{1}{4}\tilde{u}_{i+1}. \tag{67}$$

It can be interpreted as a second-order approximation of a Gaussian (thus positive) filter or as a box-filter whose characteristic length is $\hat{\Delta} = 2\Delta$ and evaluated using the trapezoidal rule.

The mixed scale model can be interpreted as a model depending on the subgrid modes using the scale similarity hypothesis [27,28] $(\tilde{u})' \approx (\widetilde{u'})$, leading to

$$q_c^2 = k, \tag{68}$$

where k is the SGS kinetic energy. This small-scale dependency of the model ensures its adaptation to the local state of the flow such that it vanishes in able results. The corresponding value of the constant C_m is 0.06, as derived from the eddy damped quasi-normal Markovian (EDQNM) theory in the isotropic case [3]. It is then to be remarked that this model is employed in the channel configuration using the theoretical value of the constant, a self-adaptive behaviour being obtained through the use of the variable q_c^2.

4.1.3. Hybrid Bardina–mixed scale model. The Smagorinsky model and the mixed scale model belong to the category of the functional models, i.e. the SGS term τ_{ij} is not directly modelled but its behaviour is described via a function whose mainly dissipative action is assumed to account for the kinetic energy cascade.

Another type of model, called the structural model, has been developed. These models are mainly based on the hypothesis, proposed by Bardina *et al.* [27,28], that the structure of a tensor built using subgrid scales is similar to those of the corresponding tensor built using the smallest resolved scales. This induces that the solution spectrum is divided in three parts: large resolved scales, small resolved scales and subgrid scales. A possible interpretation of this hypothesis is that small resolved and unresolved scales are both influenced by the large resolved scale in a similar way. The application of this model requires the extraction of small scales from the solved field. This is achieved using the test filter described in Section 4.1.2

$$\tau_{ij} \equiv \widetilde{u_i u_j} - \widetilde{u}_i \widetilde{u}_j = \widehat{\widetilde{u}_i \widetilde{u}_j} - \widehat{\widetilde{u}_i} \widehat{\widetilde{u}_j} = L_{ij}^m. \tag{69}$$

This model produces good results in *a priori* tests, at least for incompressible cases, but it underestimates the energy cascade and does not lead to stable calculations. However, it can take into account the inverse energy cascade.

The solution chosen in this work to solve this problem, is to use a hybrid model that is a linear combination of the aforementioned structural model with the mixed scale model

$$\tau_{ij}^D = \frac{1}{2}\left(-\bar{\rho} v_t S_{ij} + L_{ij}^m - \frac{1}{3} L_{kk}^m \delta_{ij} \right). \tag{70}$$

This formulation is similar to the one proposed by Erlerbacher *et al.* [6] and seems to be the best suited to take advantage of both the structural and the functional models.

4.2. Selective function

In order to improve the prediction of intermittent phenomena, a sensor based on a structural information is introduced. This modification is achieved by incorporating a selective function based on the local angular fluctuation of the vorticity, as proposed by David [29]. The basic idea is to rescale the SGS model in order to apply it only when the fundamental hypothesis of SGS modelling are fulfilled, i.e. when all the scales of the exact solution are not captured by the computation and when the flow exhibits an isotropic homogeneous turbulent behaviour. So, the problem is to check at each grid point and at each time step if these two conditions are verified or not. The structural sensor introduced by David allows the second point to be checked. To do this, one assumes that if the flow corresponds to developed turbulence, the highest resolved frequencies exhibit some proper characteristics of isotropic homogeneous turbulence, including structural properties.

On the basis of DNS of isotropic homogeneous turbulence, David pointed out that the probability density function of the local angular fluctuation of vorticity θ exhibits a peak near 20°. Consequently, he proposed to consider the flow as locally underresolved and turbulent when the local angular fluctuation of the vorticity vector of the highest resolved frequencies is higher than a given threshold angle θ_0.

The original selection function f_{θ_0} by David reads

$$f_{\theta_0}(\theta) = \begin{cases} 1 & \text{if } \theta \geq \theta_0 \\ 0 & \text{else} \end{cases}, \tag{71}$$

where θ is the angle between the local filtered vorticity ($\omega = \nabla \times \tilde{u}$) and the local averaged filtered vorticity ($\omega_m = \nabla \times \hat{\tilde{u}}$), and $\theta_0 = 20°–40°$. This function is discontinuous, and can then introduce some numerical problems. A continuous selection function is introduced [30]

$$f_{\theta_0}(\theta) = \begin{cases} 1 & \text{if } \theta \geq \theta_0 \\ r(\theta)^n & \text{else} \end{cases}, \tag{72}$$

where r is defined as

$$r(\theta) = \frac{\tan^2\left(\frac{\theta}{2}\right)}{\tan^2\left(\frac{\theta_0}{2}\right)}. \tag{73}$$

The calculations presented hereafter have been performed using $n = 2$ and $\theta_0 = 20°$.

Moreover, the angle θ can be expressed as a function of ω_m and ω' defined as $\omega' = \omega_m - \omega$ using the relation

$$\omega' = \omega_m^2 + \omega^2 - 2\omega_m\omega \cos\theta, \tag{74}$$

It becomes

$$\tan^2\theta = \frac{2\omega_m\omega - \omega_m^2 - \omega^2 + \omega'^2}{2\omega_m\omega + \omega_m^2 + \omega^2 - \omega'^2}. \tag{75}$$

As proposed by David, θ_0 is set equal to 20°, corresponding to the observed location of the peak of the density probability function for the angular variation of the local vorticity vector in the case of an isotropic homogeneous turbulence. It should be noticed that the action of the selection function is observed to be the same for $\theta_0 \in [20°, 40°]$ [P. Comte, private communication]. The sensitivity of the SGS model to the discrete test filter is investigated in Reference [31]. The modified SGS viscosity is

$$\nu_t^{(s)} = \nu_t f_{\theta_0}(\theta). \tag{76}$$

4.3. Energy equation

As shown in Section 2.2, the filtering of the energy conservation equation leads to the definition of an important number of SGS terms ($B_1, \ldots, B_7$). This section addresses the associated SGS modelling.

In order to reduce the number of SGS terms to model, Vreman *et al.* [7] compared the magnitude of the terms $B_1, \ldots, B_7$ through some *a priori* tests, in the case of a compressible shear layer for a Mach number comprised between 0.2 and 1.2. These authors concluded that terms B_6 and B_7 are two to three orders of magnitude lower than the other SGS terms in the energy equation. This result is assumed to be extendable to the case of the channel flow and these terms are neglected in the present work

$$B_6 \approx 0, \tag{77}$$

$$B_7 \approx 0. \tag{78}$$

SGS terms B_3 and B_4 are obtained in a straightforward manner reporting the expression used to model the SGS term τ_{ij} in Equations (25) and (26).

The SGS terms B_1 and B_2 are modelled following the idea proposed by Vreman *et al.* [7] and Moin *et al.* [19] to use an eddy diffusivity,

$$B_1 + B_2 = -\frac{\partial}{\partial x_j}\left(\frac{\bar{\rho} v_t}{(\gamma - 1) Pr_t M_0^2} \frac{\partial \tilde{T}}{\partial x_j}\right), \tag{79}$$

where the SGS Prandtl number Pr_t is chosen to be constant and set equal to 0.5.

In order to close the problem of SGS modelling in the filtered energy equation, one has to express the term B_5. Following studies by Ghosal *et al.* [32] and Horiuti [33], one can write

$$B_5 = C_\epsilon \bar{\rho} \frac{k^{3/2}}{\Delta}, \tag{80}$$

where the SGS kinetic energy k is given as

$$k = \frac{1}{2} \tau_{kk}. \tag{81}$$

It is important to notice that the test filter has to be positive to ensure the positivity of k and B_5 to be well-defined (see Section 4.1.2).

The term C_ϵ is computed using the relation originally proposed by Vreman *et al.* [7],

$$C_\epsilon = \frac{\int_\Omega [B_2 + B_3 + B_4] \, \mathrm{d}\vec{x}}{\int_\Omega [\bar{\rho} k^{3/2}/\Delta] \, \mathrm{d}\vec{x}}. \tag{82}$$

5. APPLICATIONS

Two applications are presented. The first case is the LES of an isothermal-wall subsonic ($M_0 = 0.5$) channel flow that corresponds to the experiments of Niederschulte *et al.* [34]. The second one deals with the LES of an isothermal-wall supersonic ($M_0 = 1.5$) channel flow that corresponds to the DNS results of Coleman *et al.* [9,35]. The computational configuration is displayed in Figure 1. The x-, y- and z-axes are along the streamwise, spanwise and the wall-normal directions respectively.

Both cases are computed for a Reynolds number, based on the bulk velocity and channel half-width, set equal to 3000.

In the periodic directions, the computational domain length is chosen to ensure that no point in space will correlate with itself through a periodic boundary. This is enforced by requiring that the computational domain be larger than the length of the longest experimentally observed coherent structures commonly called 'streaks'. These distances may be estimated *a priori* by considering Clark and Markland's [36] incompressible results, in which the streamwise extent of these structures was found to be $\lambda_l^+ \approx 440$ and the mean spanwise distance between two structures was found to be $\lambda_s^+ \approx 100$. The physical domain sizes, therefore, are $L_x = 2\pi$, $L_y = 4\pi/3$ and $L_z = 2$, such that streamwise and spanwise length of the domain expressed in wall units are, respectively, $L_x^+ \approx 1150$ and $L_y^+ \approx 760$ for the subsonic case and $L_x^+ \approx 1390$ and $L_x^+ \approx 925$ for the supersonic case. In the least favourable case, which is the supersonic one, the chosen L_x corresponds to a spatial correlation of not larger than 10%, as can de deduced from Reference [35].

For each case, two models are presented on two meshes: a Smagorinsky model corrected with a Van Driest damping function and a hybrid Bardina–selective mixed scale (HBSMS) model on both a coarse and a fine mesh. The mesh characteristics are listed in Table I. Parameters m_x, m_y and m_z are, respectively, the number of grid points in the streamwise, spanwise and wall-normal directions, while the grid spacing in viscous wall units are Δ_x^+, Δ_y^+

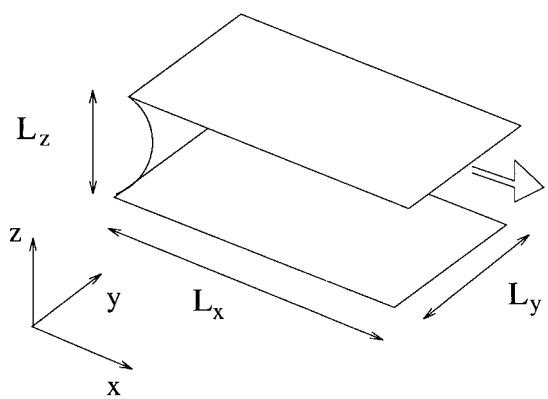

Figure 1. Configuration sketch.

Table I. Mesh characteristics

	m_x	m_y	m_z	$M_0 = 0.5$			$M_0 = 1.5$		
				Δ_x^+	Δ_y^+	Δ_z^+	Δ_x^+	Δ_y^+	Δ_z^+
Coarse mesh	21	41	119	57	20	1	69	23	1
Fine mesh	41	65	119	30	12	1	35	14	1

and Δ_z^+ listed for both the subsonic and the supersonic case. Refinement occurs only in the streamwise and spanwise directions, while the number of grid points in the wall-normal direction is kept constant. The coarse mesh, therefore, contains roughly three times less points than the fine one. Note that for both cases, uniform grid spacing is used in the streamwise and spanwise directions and a mesh refinement following an hyperbolic tangent law is used in the wall-normal direction. The first grid point off the wall is roughly located at $z^+ \approx 1$ for both meshes.

The statistical moments have been computed by performing the average over homogeneous planes parallel to the walls and over 20000 time steps, corresponding to 17×10^6 samples, on the coarse mesh and over 15000 time steps, corresponding to 40×10^6 samples, for the fine mesh. The associated averaging period corresponds to 50 dimensionless time units (based on bulk velocity and channel half-width) for the $M_0 = 1.5$ case on the coarse grid, corresponding to 3.1 time wall units. The period is reduced to 40 for the $M_0 = 0.5$ case on the coarse grid (2.4 time wall units) and the $M_0 = 1.5$ case on the fine grid (2.5 time wall units). For the $M_0 = 0.5$ case on the fine grid, the period is only 30 in dimensionless time (1.8 time wall units). Periods of 30, 40 and 50 roughly correspond to 5, 6.5 and 8 crosses through the channel respectively.

5.1. Subsonic case

5.1.1. Computational parameters. The Reynolds number is set equal to 3000 and the reference Mach number is set equal to 0.5. Because the Mach number is lower than 0.6, this case is expected to follow a quasi-incompressible pattern. This is in agreement with Ridder *et al.* [15], who observed this quasi-incompressible behaviour for Mach numbers up to 0.7 on the channel flow configuration. Results are compared with the experimental results of Niederschulte *et al.* [34], the experimental data of Kreplin and Eckelmann [37] and the DNS data of Kim *et al.* [38], which are partially available. Both a coarse and a fine mesh are presented with the Smagorinsky and the HBSMS models.

In their simulation, Kim *et al.* used a computational domain corresponding to the volume $L_x \times L_y \times L_z$, with $L_x = 4\pi$, $L_y = 2$, and $L_z = 2$. In order to capture all turbulent structures they also used a very fine mesh: in the streamwise and spanwise directions, grid spacings are respectively $\Delta_x^+ \approx 12$ and $\Delta y^+ \approx 7$. In the wall-normal direction, the first grid point in the simulation by Kim *et al.* was located at $z^+ = 0.05$. This is to be compared with the meshes presented in this work (see Table I). The coarser grid corresponds to a reduction, by a factor 13, of the total number of grid points for an equivalent computational domain size, when compared with the DNS.

As emphasized in the previous section, the Smagorinsky constant is set to 0.1, while the mixed scale model constant is set to 0.06, which is the value derived from the EDQNM isotropic closure [3]. It should be noticed that with these values of the constants, the HBSMS model is supposed to be four times more dissipative than the Smagorinsky model for the isotropic turbulence case.

5.1.2. Results and discussion. Table II summarizes the mean flow variables for all presented cases. Except for the HBMSM model on the coarse mesh, the centreline velocities are within 1% of the value of 1.157 given by Dean's [39] correlation, given by

$$\langle U_c \rangle = 1.28(2Re)^{-0.0116}. \tag{83}$$

The smallest relative error of 0.3% is observed on the coarse mesh using the Smagorinsky model, while the HBSMS model on the coarse mesh leads to a relative error of 1.44%. It is noticed that these values are also in very good agreement with the value of 1.16 given by Niederschulte *et al.* [34].

The skin friction coefficients C_f are also in very good agreement with the value of 8.29×10^{-3} given by Dean's correlation of

$$C_f = 0.073(2Re)^{-0.25}. \tag{84}$$

Best estimations of the C_f coefficient are observed for the HBMSM model, with relative errors of 4.9% on the coarse mesh and 4.8% on the fine mesh. The Smagorinsky model leads to a relative error of 10.6% on the coarse mesh and 13.85% on the fine one. It is noticed that a larger error is committed on the fine mesh than on the coarse one when using the Smagorinsky model. This tends to illustrate the fact that the HBSMS model better captures the physics of the flow, even on a coarse mesh. Similar observations can be made when comparing obtained values with the 8.28×10^{-3} value given by Niederschulte *et al.*

Table II also gives the ratio of the centreplane temperature to the wall temperature T_c/T_w and the ratio of the centreplane density to the wall density ρ_c/ρ_w. One can see very few discrepancies between the different presented cases: variation occurs only on the third decimal for both the temperature and the density ratio.

The mean streamwise velocity profiles are illustrated in Figure 2 as a comparison with the DNS data of Kim *et al.* [38] and the experimental data of Niederschulte *et al.* [34]. One can

Table II. Mean flow variables, subsonic case

	Smagorinsky (coarse mesh)	HBSMS (coarse mesh)	Smagorinsky (fine mesh)	HBSMS (fine mesh)
$\langle U_c \rangle$	1.1605	1.1405	1.1630	1.1653
U^*	5.9627×10^{-2}	6.4585×10^{-2}	5.8521×10^{-2}	6.4547×10^{-2}
C_f	7.418×10^{-3}	8.703×10^{-3}	7.1454×10^{-3}	8.693×10^{-3}
T_c/T_w	1.045	1.044	1.047	1.047
ρ_c/ρ_w	0.956	0.956	0.955	0.956

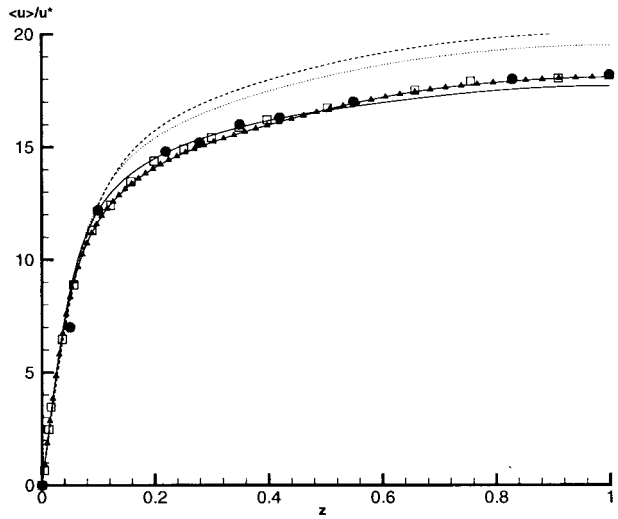

Figure 2. Mean streamwise velocity profile normalized with the skin friction velocity: ●, DNS of Kim *et al.*; □, experimental data of Nierdershulte *et al.*; . . . ., Smagorinsky (coarse mesh); ----, Smagorinsky (fine mesh); —, HBMSM (coarse mesh); –▲–, HBMSM (fine mesh).

observe that for the two grids, the HBSMS model better fits the reference data than the Smagorinsky model: the maximal relative error observed for the HBSMS model is less than 1%, while it is 10.45% for the Smagorinsky model on the fine mesh. The Smagorinsky model leads to an overprediction of the centreline mean velocity, due to the overdissipative behaviour, leading to an underprediction of the skin friction velocity U^*.

It is noticed that when considering the HBSMS model, mesh refinement does not correspond to a significant improvement of the results. On the other hand, mesh refinement induces a larger relative error when considering the Smagorinsky model. This is in agreement with conclusions drawn from the analysis of the results related to the skin friction coefficient (see Table II).

Figure 3 illustrates curve fits of the compressible LES data in the viscous sublayer and in the logarithmic region of the boundary layer. Results are plotted in wall units. All the models for both coarse and fine meshes show excellent agreement with the linear $u^+ = z^+$ law in the viscous sublayer ($z^+ \leq 5$). In the logarithmic region, the square-marked line corresponds to the theoretical logarithmic law. One can observe that both on the coarse and on the fine mesh, the HBSMS model better fits the theoretical law than the Smagorinsky model. This is in agreement with what is observed in Figure 2.

The mean temperature and density profiles are presented in Figures 4 and 5. Because boundary conditions are of isothermal type, the mean temperature variation is found to be qualitatively different than that found in adiabatic-wall boundary conditions. The maximum temperature and minimum density are located on the centreline of the channel, while the walls

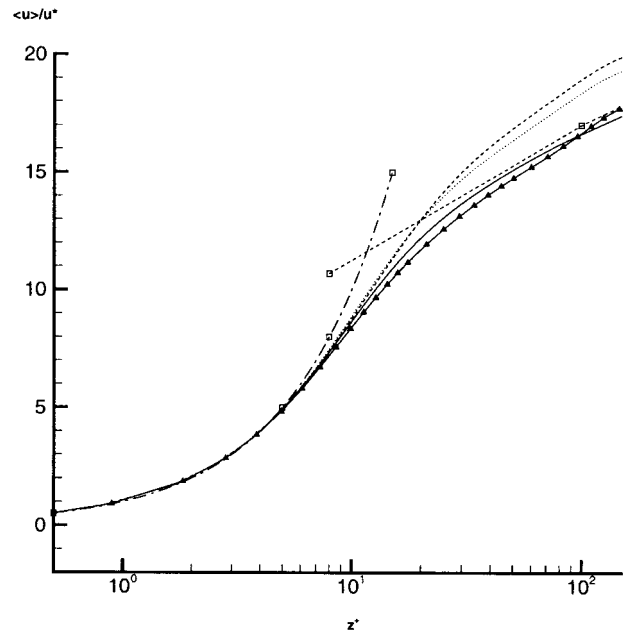

Figure 3. Curve fit of mean velocity profiles in viscous sublayer and logarithmic region: - -□- -, $u^+ = 2.5 \ln z^+ + 5.5$; - · □ · -, $u^+ = z^+$; . . . ., Smagorinsky (coarse mesh); ----, Smagorinsky (fine mesh); —, HBMSM (coarse mesh); –▲–, HBMSM (fine mesh).

are colder than the core of the flow. This is due to the fact that heat generated by the dissipation is allowed to be transferred out of the channel. It is noticed that almost no difference can be observed between either the different meshes or the different models. All the simulations lead to a value nearly equal to 1.05 in the centre of the channel for the temperature and slightly lower than 1.0 for the density. This illustrates the fact that mean temperature and density profiles are not appropriate values to compare effects of the model or the mesh on the results of a simulation.

Figure 6 shows the mean pressure profiles. The mean flow is approximately isobaric, and the mean wall-normal pressure gradient is very small. One also can observe that the use of a fine mesh tends to increase the mean value of the pressure in the channel.

Figure 7 compares the resolved streamwise turbulence intensity to the experimental data of Niederschulte *et al.* and the DNS data of Kim *et al.* The overdissipative character of the Smagorinsky model leads to a large overprediction of the results in the near-wall region, with 12.5% of relative error on the fine mesh. The relative error is even larger on the coarse mesh. This is in agreement with the observations of Najjar and Tafti [40].

On the coarse grid, the HBSMS model yields a good agreement with the reference data as the value of the peak is correctly predicted (within 10% of the relative error) although it slightly underpredicts the value of normalized velocity fluctuations in the centre of the channel.

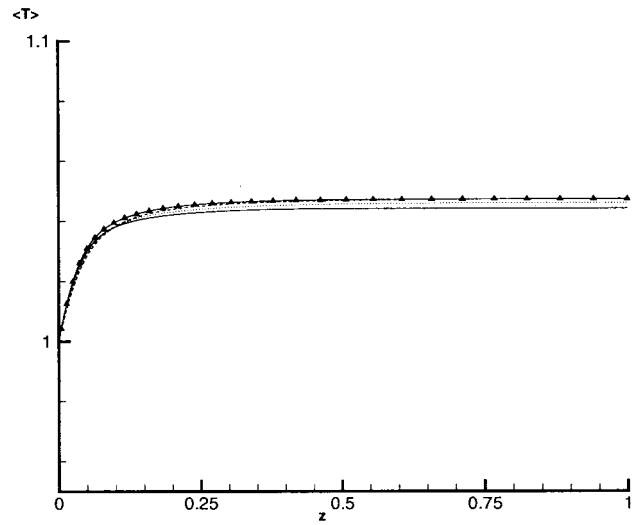

Figure 4. Mean temperature profile: . . . ., Smagorinsky (coarse mesh); ----, Smagorinsky (fine mesh); —, HBMSM (coarse mesh); –▲–, HBMSM (fine mesh).

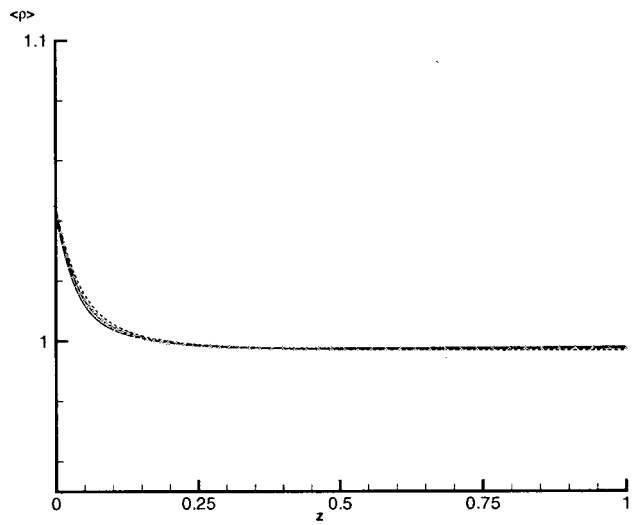

Figure 5. Mean density profile: . . . ., Smagorinsky (coarse mesh); ----, Smagorinsky (fine mesh); —, HBMSM (coarse mesh); –▲–, HBMSM (fine mesh).

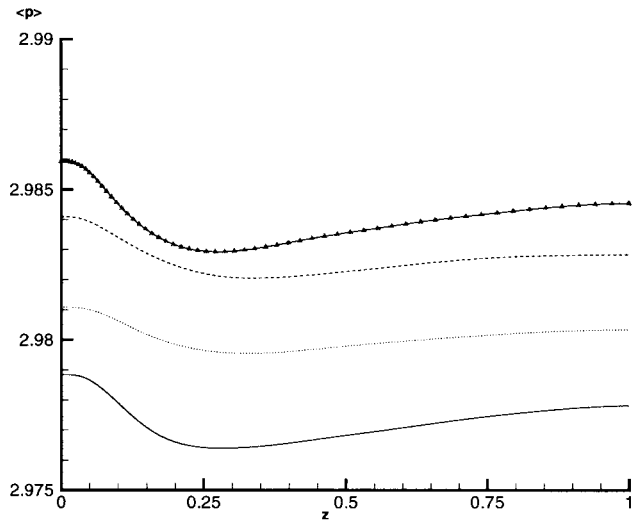

Figure 6. Mean pressure profile: . . . ., Smagorinsky (coarse mesh); ----, Smagorinsky (fine mesh); —, HBMSM (coarse mesh); –▲–, HBMSM (fine mesh).

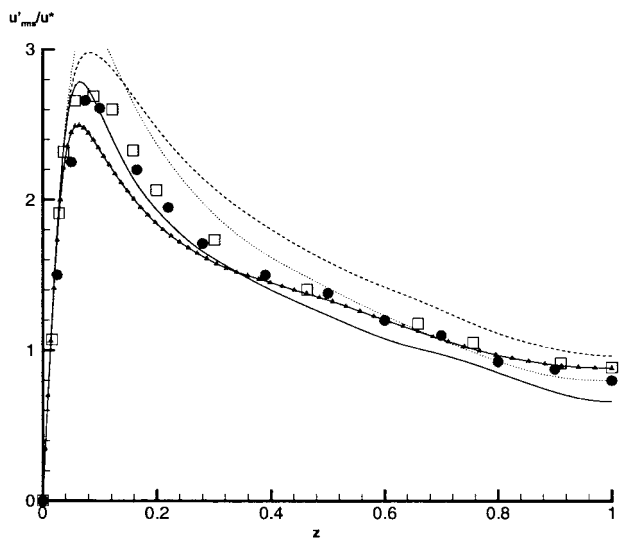

Figure 7. Streamwise r.m.s. velocity fluctuations normalized with the skin friction velocity: ●, DNS of Kim *et al.*; □, experimental data of Nierdershulte *et al.*; . . . ., Smagorinsky (coarse mesh); ----, Smagorinsky (fine mesh); —, HBMSM (coarse mesh); –▲–, HBMSM (fine mesh).

Refining the mesh leads to an improvement of the prediction of the peak value for the Smagorinsky model but it is still too dissipative, while the underprediction of the peak shows the HBSMS model is slightly underdissipative.

Figures 8 and 9 illustrate the spanwise and the wall-normal velocity fluctuations normalized with the skin friction velocity as compared with the DNS by Kim *et al.* and with the experimental results of Niederschulte *et al.*, when data are available. The physical behaviour is successfully predicted by both the Smagorinsky and the HBSMS models on the finest mesh. The Smagorinsky model gives better predictions in the centreline of the channel, while the HBSMS model leads to an underprediction of roughly 9.5%. Furthermore, it can be observed that mesh refinement leads to an improvement for both models.

It is interesting to remark that a much better agreement with reference data is obtained when the resolved Reynolds stresses are renormalized using the mean velocity rather than the friction velocity (not shown here). This is due to the fact that the error committed on the mean velocity is much less important than those observed on the wall shear stress.

The shear stress normalized with the square of the skin friction velocity is presented in Figure 10. Good agreement is generally seen to occur in the core region of the channel, except for the HBSMS model on the coarse mesh, which also leads to an underprediction of the value of the peak with a level of relative error equal to 26%. Although it is clear that refining the mesh leads to an increase of the peak for both the Smagorinsky and the HBSMS models, it is very difficult to determine which model gives the best result for the shear stress as long as large discrepancies are observed between the data of Niederschulte *et al.* and Kim *et al.* This can be attributed to noise and high frequency non-turbulent pressure oscillations in the experiment of Niederschulte *et al.*

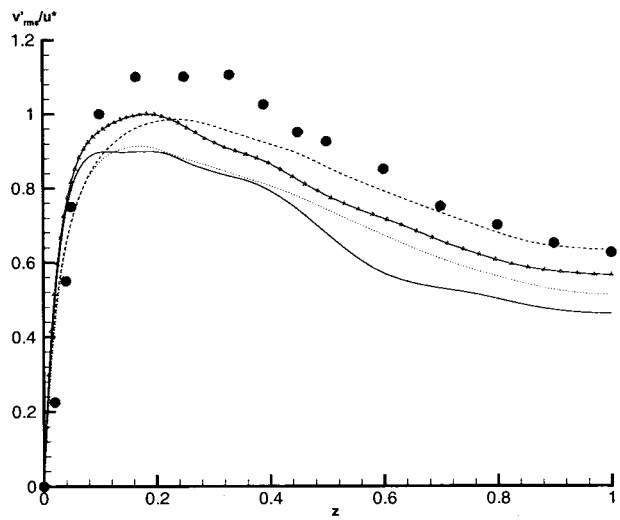

Figure 8. Spanwise r.m.s. velocity fluctuations normalized with the skin friction velocity: ●, DNS of Kim *et al.*; □, experimental data of Nierdershulte *et al.*; . . . ., Smagorinsky (coarse mesh); ----, Smagorinsky (fine mesh); —, HBMSM (coarse mesh); –▲–, HBMSM (fine mesh).

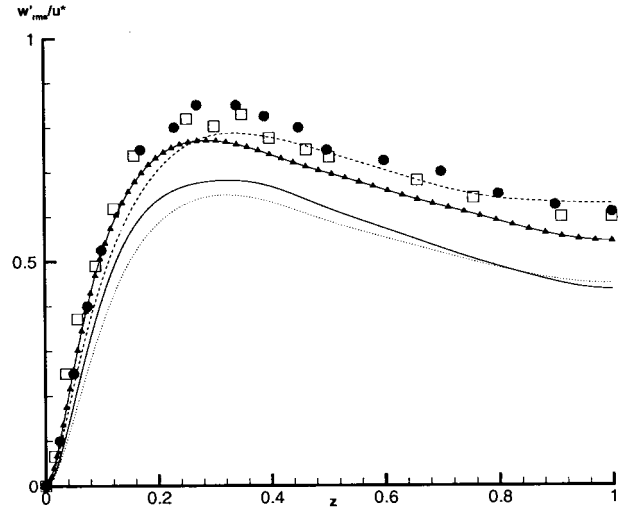

Figure 9. Wall-normal r.m.s. velocity fluctuations normalized with the skin friction velocity: ●, DNS of Kim *et al.*; □, experimental data of Nierdershulte *et al.*; . . . ., Smagorinsky (coarse mesh); ----, Smagorinsky (fine mesh); —, HBMSM (coarse mesh); –▲–, HBMSM (fine mesh).

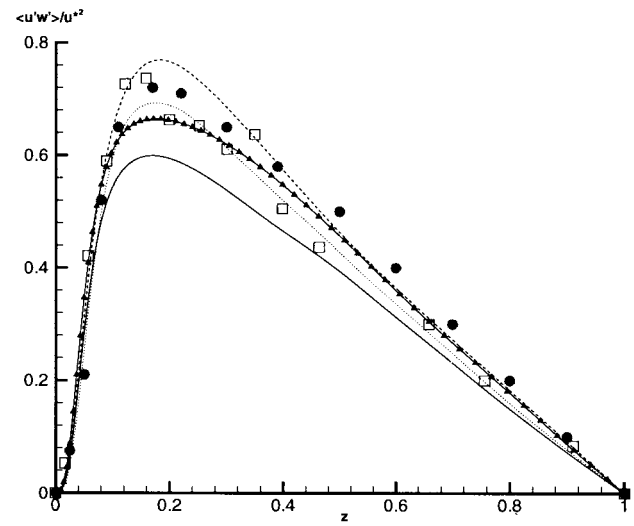

Figure 10. Shear stress normalized with the square of the skin friction velocity: ●, DNS of Kim *et al.*; □, experimental data of Nierdershulte *et al.*; . . . ., Smagorinsky (coarse mesh); ----, Smagorinsky (fine mesh); —, HBMSM (coarse mesh); –▲–, HBMSM (fine mesh).

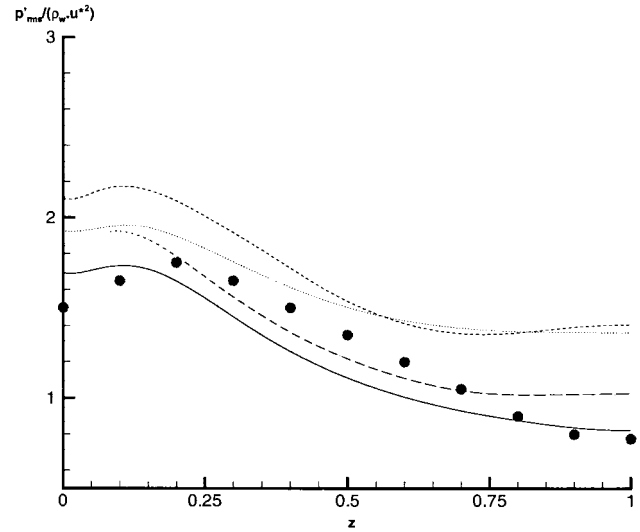

Figure 11. r.m.s. pressure fluctuations: ●, DNS of Kim *et al.*; □, experimental data of Nierdershulte *et al.*; . . . ., Smagorinsky (coarse mesh); ----, Smagorinsky (fine mesh); —, HBMSM (coarse mesh); –▲–, HBMSM (fine mesh).

The mean root-mean-squared (r.m.s.) fluctuations of pressure are presented in Figure 11 and compared with the data of Kim *et al.* All simulations underestimate the location of the peak. The r.m.s. wall pressure fluctuation is significantly lower than results determined experimentally in the literature. For example, Willmarth [41] reports a wall value of 2.64, while Elliot [42] reports 2.6. It should be noticed that in their simulation, Ridder and Bedini [15] also reported an underestimated value of 1.4 for the mean r.m.s. fluctuation of pressure. Kim *et al.* suggest that there is a Reynolds number dependence and point to Willmarth's review [41] as evidence.

Finally, Figures 12 and 13 show the resolved r.m.s. density and temperature fluctuations. Almost no difference can be observed between the Smagorinsky model and the HBSMS model on the fine mesh, although the HBSMS model leads to a slightly smaller value of the peak. One can observe using the coarse mesh leads to a larger prediction of the value of the peak both for the r.m.s. density and the temperature fluctuations, but contrary to what occurs on the fine mesh, larger values are predicted using the Smagorinsky model than the HBSMS model.

5.2. Supersonic case

5.2.1. Computational parameters. The parameters of the simulations are set equal to those of the reference DNS by Coleman *et al.* [9]: the Reynolds number is equal to 3000 as in the subsonic case, while the reference Mach number is raised to 1.5. It is recalled that the computational domain corresponds to the volume $L_x \times L_y \times L_z$, with $L_x = 2\pi$, $L_y = 4\pi/3$ and $L_z = 2$. The same dimensions were used for the DNS, with an exception for the streamwise length, which is halved in the present case.

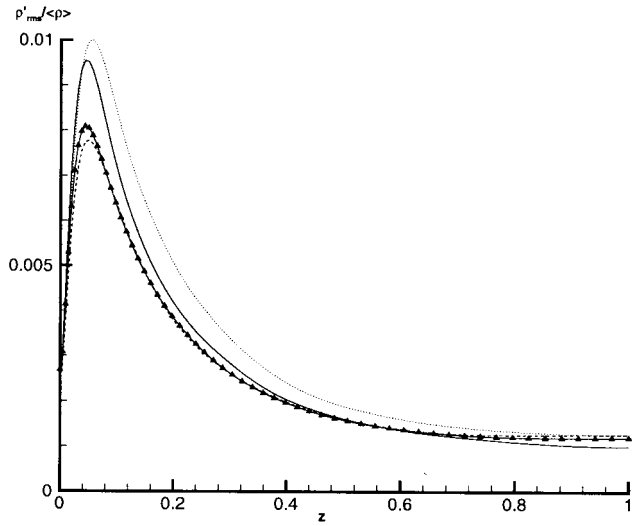

Figure 12. r.m.s. density fluctuations normalized with the mean density profile: . . . ., Smagorinsky (coarse mesh); ----, Smagorinsky (fine mesh); —, HBMSM (coarse mesh); –▲–, HBMSM (fine mesh).

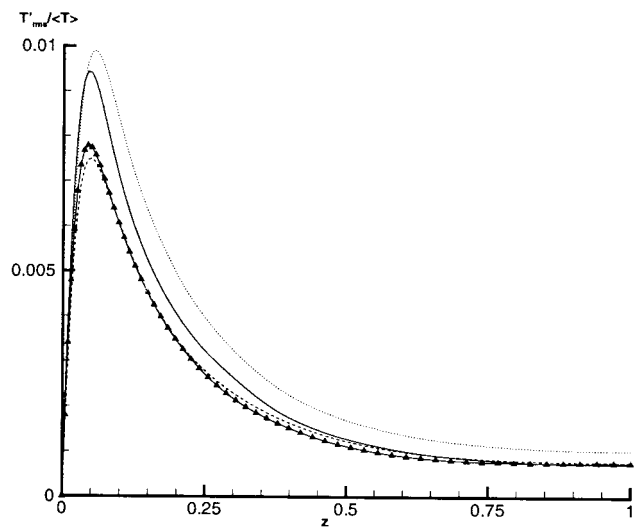

Figure 13. r.m.s. temperature fluctuations normalized with the mean temperature profile: . . . ., Smagorinsky (coarse mesh); ----, Smagorinsky (fine mesh); —, HBMSM (coarse mesh); –▲–, HBMSM (fine mesh).

The presented results are compared with those from the DNS by Coleman *et al.* [9]. In their simulations, in order to capture all turbulent structures, Coleman *et al.* did use a very fine mesh, corresponding to x and y grid spacing in viscous wall units equal to $\Delta x^+ \approx 19$ and $\Delta y^+ \approx 12$. In the wall-normal direction, the first collocation point was approximately $z^+ \approx 0.1$. This is to be compared with the meshes presented in this work (see Table I): the coarser grid corresponds to a reduction by a factor 15 of the total number of grid points when compared with the DNS results by Coleman *et al.*

5.2.2. Results and discussion. Table III summarizes the mean flow variables for all presented cases. One can notice that values of the friction velocity are slightly lower than those obtained in the subsonic case. In a similar way, the mean value of the ratio of the centreline density to the wall density decreases when the Mach number is increased. This induces an increase from approximately 1.04 to 1.4 of the mean ratio of the centreplane temperature to the wall temperature. One can observe that refining the mesh leads to better results for both the Smagorinsky and the HBSMS model except for the skin friction velocity U^*: the relative errors are 12.3% and 11.9% on the coarse mesh for the Smagorinsky and the HBSMS model respectively, while they are 19.4% and 13.8% on the fine mesh. When considering the fine mesh, one can observe the HBSMS model leads to better estimation of the listed values except for the ratio of the centreplane temperature to the wall-temperature: relative error is 0.07% using the Smagorinsky model while it is 1.1% using the HBSMS model. Furthermore, the largest discrepancy is observed on the skin friction velocity with a relative error estimated equal to 19.4% on the coarse mesh using the Smagorinsky model. It is remarked that skin friction does not exhibit grid convergence, regardless that all the others quantities do. This may be attributed to an insufficient adaptation of the SGS models to the local state of the flow in the viscous sublayer, and especially to strong anisotropy and equilibrium, leading to a bad prediction of the velocity gradient.

Mean profiles of the streamwise velocity component and density are compared with the DNS data respectively in Figures 14 and 15. As in the subsonic case, good agreement is achieved for both the coarse and the fine mesh and for the two presented models. One can observe that the plotted curves are almost superposed for the mean streamwise velocity and the mean density, and therefore are almost indistinguishable.

The mean temperature profiles are compared with the DNS reference in Figure 16. In the near-wall region, the best results are obtained using a Smagorinsky model on a coarse mesh. In the centre of the channel, results are in good agreement with the value ($\langle T \rangle = 1.38$) computed by Coleman *et al.* The greatest relative error is committed using the Smagorinsky

Table III. Mean flow variables, supersonic case

	Smagorinsky (coarse mesh)	HBSMS (coarse mesh)	Smagorinsky (fine mesh)	HBSMS (fine mesh)	DNS (Coleman *et al.*)
$\langle U_c \rangle$	1.1901	1.1554	1.1752	1.1752	1.1681
U^*	5.5524×10^{-2}	5.5774×10^{-2}	5.1031×10^{-2}	5.4532×10^{-2}	6.3285×10^{-2}
T_c/T_w	1.366	1.417	1.379	1.393	1.378
ρ_c/ρ_w	0.7142	0.7139	0.7166	0.723	

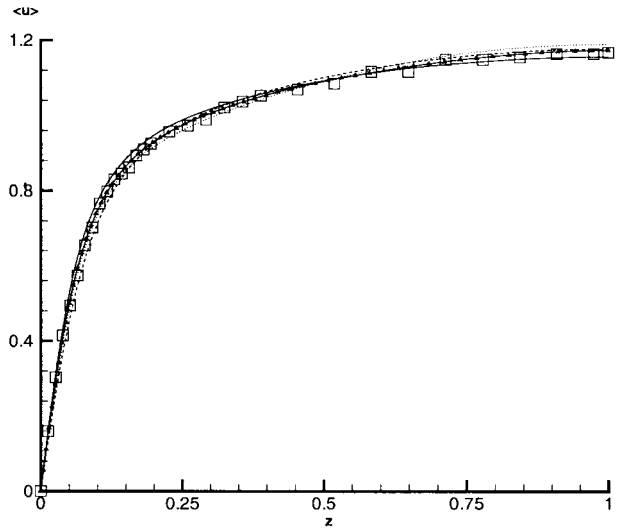

Figure 14. Mean streamwise velocity profile: □, DNS of Coleman *et al.*; . . . ., Smagorinsky (coarse mesh); ----, Smagorinsky (fine mesh); —, HBMSM (coarse mesh); –▲–, HBMSM (fine mesh).

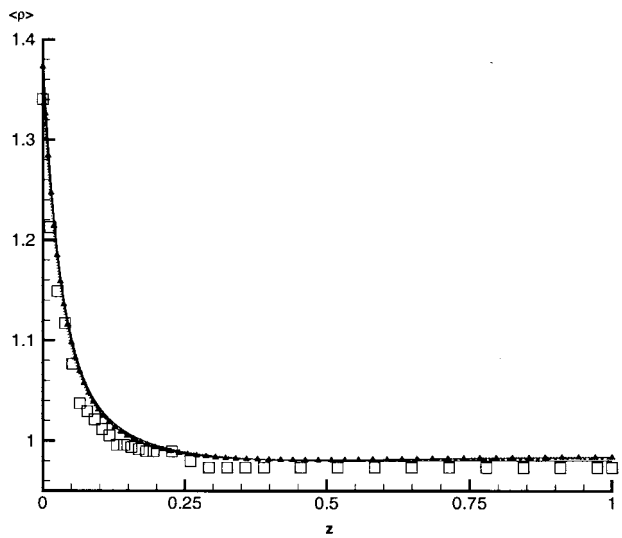

Figure 15. Mean density profile: □, DNS of Coleman *et al.*; . . . ., Smagorinsky (coarse mesh); ----, Smagorinsky (fine mesh); —, HBMSM (coarse mesh); –▲–, HBMSM (fine mesh).

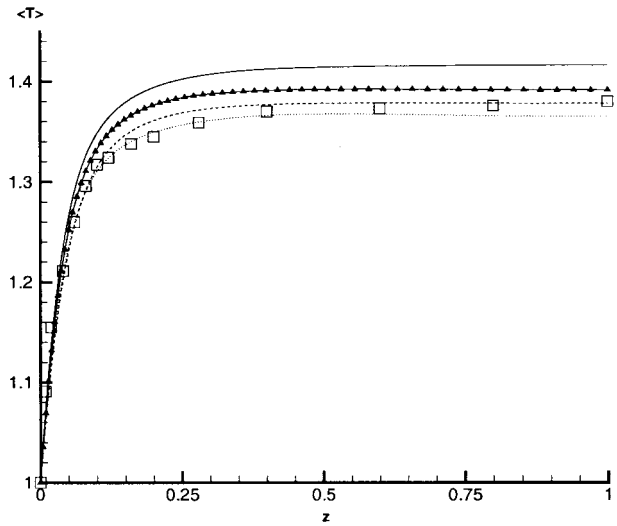

Figure 16. Mean temperature profile: □, DNS of Coleman *et al.*; . . . ., Smagorinsky (coarse mesh); ----, Smagorinsky (fine mesh); —, HBMSM (coarse mesh); –▲–, HBMSM (fine mesh).

model on the fine mesh. It is noticed that the HBSMS model also gives very good results on the fine mesh in the centre of the channel: relative errors are 0.1% and 0.8% for the Smagorinsky model and the HBSMS model respectively.

Figures 17 and 18 illustrate the r.m.s. of the density fluctuations normalized with the mean density and the r.m.s. of the temperature fluctuations normalized by the mean temperature. Almost no difference can be detected between the Smagorinsky model and the HBSMS model on the fine mesh: they both predict the location and the value of the peak within 1% of the relative error. The value of the peak is in very good agreement with the reference data by Coleman *et al.*, although the predicted value with the Smagorinsky model are slightly smaller in the region $z \leq 0.5$. Simulations achieved using the coarse grid lead to a large overprediction of the value of the peak, the largest error being committed using the HBSMS model: 27.5% of the greatest relative error on the density fluctuations. This is probably due to the underdissipative character of the model compared with the Smagorinsky model.

Figure 19 shows a comparison of the mean streamwise velocity fluctuations normalized with the bulk velocity with the reference data. In the near-wall region on the coarse mesh almost no difference is observed between the two presented models: they both overestimate the value of the peak with a relative estimated error of 32%. On the fine mesh, the error committed on the evaluation of the peak value is widely decreased: 2.5% for the Smagorinsky model and 3.75% for the HBSMS Model. Although these values are very small, one can observe the estimated value is slightly smaller with the HBSMS Model. Differences between the two models tend to disappear as the centre of the channel is considered.

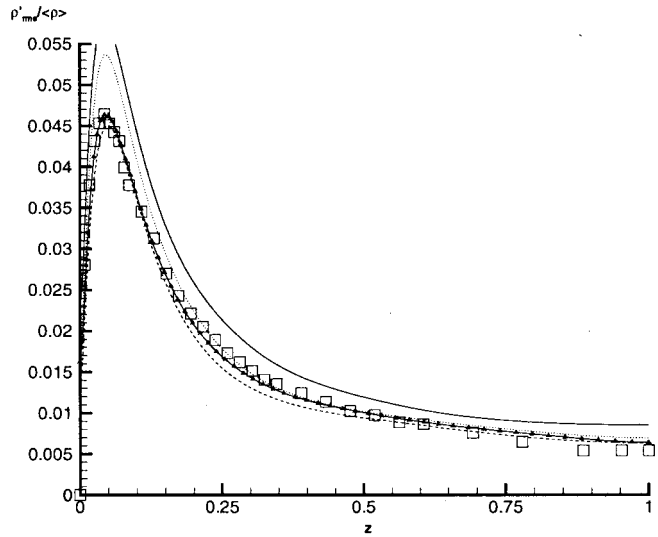

Figure 17. r.m.s. density fluctuations normalized with the mean density profile: □, DNS of Coleman *et al.*; . . . ., Smagorinsky (coarse mesh); ----, Smagorinsky (fine mesh); —, HBMSM (coarse mesh); –▲–, HBMSM (fine mesh).

Figure 20 illustrates the comparison of the mean wall-normal velocity fluctuations normalized with the bulk velocity with the DNS data. It is observed that both models lead to a correct prediction of the location of the peak with an overestimation of its value when considering the Smagorinsky model and an underestimation when considering the HBSMS model. The best prediction of the peak's value is given using the HBSMS model on a fine mesh with a greatest relative error of 8.65%. One can also notice that the Smagorinsky model gives better results when considering a coarse mesh while it is the opposite for the HBSMS model. In the centre of the channel, all models and meshes used lead to large discrepancies with the DNS results of Coleman *et al.*; moreover, they give rise to positive mean fluctuations except for the HBSMS model on the coarse mesh.

Figure 21 compares the correlation coefficient of the Reynolds stress with the DNS data of Coleman *et al.* This ratio is supposed to be approximately independent of the Mach number and to agree with its incompressible counterpart. As a matter of fact, the presented curves are very similar to those established for the $M_0 = 0.5$ case. As in this latter case, all simulations lead to an overprediction of the peak's value and its location. On a coarse mesh, the HBSMS model leads to better results with a lower overestimation of the peak: 5.4% of relative error versus 12.3% for the Smagorinsky model. Furthermore, the HBSMS model results present excellent agreement with the reference data in the centre of the channel. On the fine mesh, results are exactly the opposite: the Smagorinsky model leads to a better estimation of the peak's value and also better fit reference data in the centre of the channel.

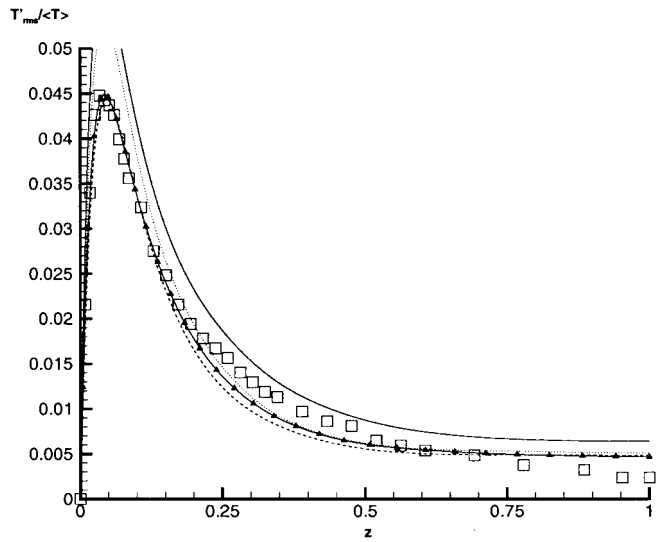

Figure 18. r.m.s. temperature fluctuations normalized with the mean temperature profile: □, DNS of Coleman *et al.*; . . . ., Smagorinsky (coarse mesh); ----, Smagorinsky (fine mesh); —, HBMSM (coarse mesh); – ▲ –, HBMSM (fine mesh).

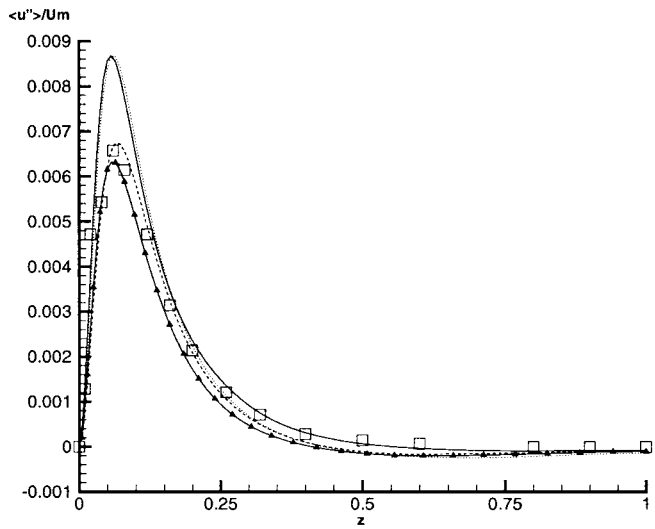

Figure 19. Streamwise velocity Favre fluctuations: □, DNS of Coleman *et al.*; . . . ., Smagorinsky (coarse mesh); ----, Smagorinsky (fine mesh); —, HBMSM (coarse mesh); – ▲ –, HBMSM (fine mesh).

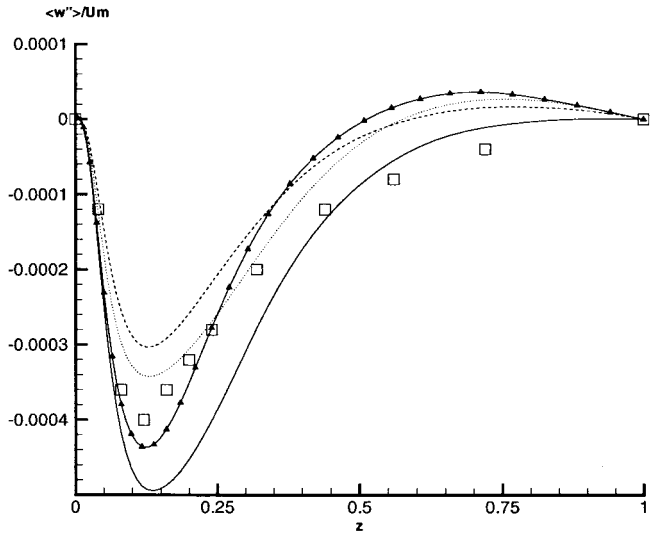

Figure 20. Wall-normal velocity fluctuations: □, DNS of Coleman *et al.*; . . . ., Smagorinsky (coarse mesh); ----, Smagorinsky (fine mesh); —, HBMSM (coarse mesh); –▲–, HBMSM (fine mesh).

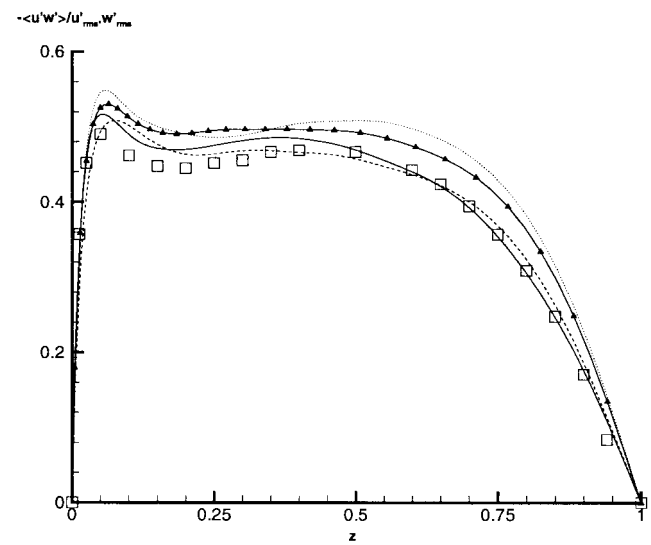

Figure 21. Correlation coefficients of the Reynolds stress: □, DNS of Coleman *et al.*; . . . ., Smagorinsky (coarse mesh); ----, Smagorinsky (fine mesh); —, HBMSM (coarse mesh); –▲–, HBMSM (fine mesh).

Another ratio, which is supposed to be independent of the Mach number, is the mixing length presented in Figure 22. On the coarse mesh, both the Smagorinsky and the HBSMS models lead to large discrepancies with the reference data of Coleman *et al.* in the centre of the channel, but not in the same way: the Smagorinsky model underestimates the right value while the HBSMS model overestimates it. In the region of the channel ranging between $z = 0$ and $z = 0.32$ on the coarse mesh, the HBSMS model gives better results with a greater relative error estimated to be 6.3% compared with the 20% estimated for the Smagorinsky model in the same region on the same mesh. Refining the mesh yields a significant improvement of the results for both models: an especially good agreement with the experimental data of Coleman *et al.* is observed for the HBSMS model. The maximal relative error is estimated to be 9%.

Figure 23 illustrates the streamwise velocity component on three perpendicular planes. Important wall layer structures are observed. These commonly called 'streaks' correspond to bands of low momentum fluid close to the wall and have been experimentally observed by many researchers [15]. The mean spanwise distance between the streaks has been found to be of the order of $\lambda^+ \approx 100$ wall units, and corresponds to the experimentally measured one. Theses regions demonstrate the bursting process of the low momentum streaks as they lift away from the wall. These regions are seen in Figure 23 on the xz-plane to be lifting away from the wall at a shallow angle.

5.3. Conclusions

LES of wall-bounded compressible flows have been performed on a periodic isothermal-wall channel configuration. Convective terms are written in skew-symmetric form and discretized

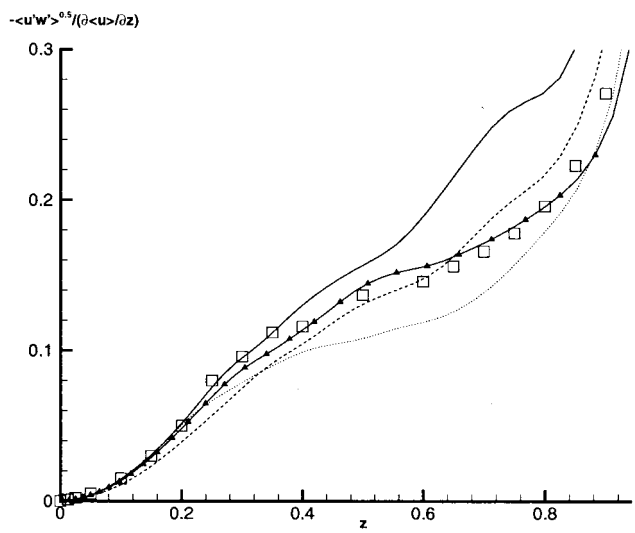

Figure 22. Mixing length: □, DNS of Coleman *et al.*; . . . ., Smagorinsky (coarse mesh); ----, Smagorinsky (fine mesh); —, HBMSM (coarse mesh); –▲–, HBMSM (fine mesh).

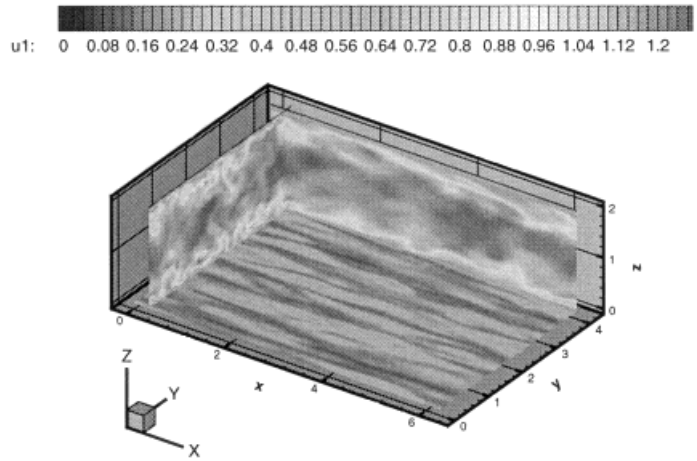

Figure 23. Iso-streamwise velocity surfaces.

using a centred fourth-order-accurate finite difference scheme, while diffusion terms were discretized via a second-order-accurate scheme. Two cases, a subsonic ($M_0 = 0.5$) and a supersonic ($M_0 = 1.5$) one, are considered. In order to analyse the influence of the mesh resolution, simulations are carried out on two different meshes. Two SGS models are tested. The first one is an extension of the Smagorinsky model for compressible flows, while the second one, referred to as the HBSMS model, is based on both large and small scales of turbulence. Various comparisons are made with experimental and DNS data at similar Reynolds number, including higher-order statistics and spatial correlations.

The method has proved its capability to simulate turbulent Poiseuille flows for subsonic and supersonic regimes. Good agreement of the results is generally observed with the reference data both for mean and fluctuating quantities. On the whole, discrepancies are estimated to be within 10–15% except for some specific quantities, such as correlation coefficients in the subsonic case using the Smagorinsky model or skin friction velocity in the supersonic case also using the Smagorinsky model.

One can observe, whenever reference data are available, that mean velocity, temperature and density maxima are overpredicted for almost all presented runs: the maximal relative error is 10.45% and is observed on the mean velocity profile (Figure 2). This is also the case for the Reynolds stresses. In the opposite way, spanwise and wall-normal velocity fluctuations are underestimated whatever the mesh or the SGS model used for the simulation.

It is observed that mesh refinement generally has only a slight influence on the mean properties of the flow both in the subsonic and the supersonic case. Although, this must be moderated when dealing with the friction velocity U^*, which does not exhibit grid convergence in all the presented simulations.

As can be expected, fluctuating properties, such as velocity, temperature or density fluctuations, are very sensitive to the mesh resolution. For the two Mach numbers considered in this

work, it is shown that improvement of the quality of the results can be reached by increasing the total number of grid points. An exception is observed for the correlation coefficients of the Reynolds stress whose estimation is worst on the fine mesh in the subsonic case using the Smagorinsky model.

Another important point is to determine the sensitivity of the results to the SGS models. In the subsonic case, the results tend to demonstrate that using the Smagorinsky or the HBSMS model leads to similar results on the mean thermodynamical parameters of the flow. This indicates that temperature and density profiles may be inappropriate values to compare effects of the model. Concurrently, it is to notice that when considering mean quantities related to the velocity, such as mean velocity profile or skin friction coefficient, the use of the HBSMS model yields the best results. Still considering the subsonic case, the HBSMS model is generally superior to the Smagorinsky model for estimating fluctuating properties of the flow. Nevertheless, if one is interested in the shear stress or the spanwise fluctuating velocity, the Smagorinsky model is better adapted.

In the supersonic case, one can observe that the Smagorinsky model leads to the best prediction of the thermodynamical properties but, as in the subsonic case, if one is interested in estimation of the skin friction velocity U^*, one should prefer the HBSMS model. Nevertheless, one should be extremely cautious with these conclusions as long as the value of the constants used in the presented model play an important role. One should keep in mind that the value of 0.1 set for the Smagorinsky model (56) leads to an eddy viscosity roughly four times less dissipative than the HBSMS model for the isotropic turbulence case. Furthermore, it is important to remember that all presented results have been obtained neglecting SGS terms B_6 and B_7 in the filtered energy conservation equation (21).

Concerning the supersonic case, fluctuating quantities related to the velocity show better agreement with the reference data when using the Smagorinsky model. However, fluctuating thermodynamical quantities seem to be less sensitive to the SGS model.

As an overall conclusion, the HBSMS model is a more advisable choice when considering the subsonic case, while it does not lead to any significant improvement of the results in the supersonic case, except if one is interested in the skin friction velocity estimation.

The last important conclusion that can be drawn from this work is that mean temperature and mean density appear to be less sensitive to the SGS model and the grid resolution than the mean quantities based on the velocity.

ACKNOWLEDGMENTS

Miss F. Roi is gratefully acknowledged for her contribution to the analysis of the data. This work was supported by the Ministry of Defence /SPAé.

REFERENCES

1. M. Lesieur and O. Metais, 'New trends in large eddy simulations of turbulence', *Annu. Rev. Fluid Mech.*, **28**, 45–82 (1996).
2. R.S. Rogallo and P. Moin, 'Numerical simulation of turbulent flows', *Annu. Rev. Fluid Mech.*, **16**, 99–137 (1984).
3. P. Sagaut, *Introduction à la Simulation des Grandes Échelles pour les Écoulements de Fluide Incompressible*, Springer, Berlin, 1998.

4. C. Härtel, L. Kleiser, F. Unger and R. Friedrich, 'Subgrid-scale energy transfer in the near wall region of turbulent flows', *Phys. Fluids*, **6**, 3130–3143 (1994).
5. F. Ducros, P. Comte and M. Lesieur, 'Large eddy simulation of transition to turbulence in a boundary layer developing spatially over a flat plate', *J. Fluid Mech.*, **326**, 1–36 (1996).
6. G. Erlerbacher, M.Y. Hussaini, C.G. Speziale and T.A. Zang, 'Toward the large eddy simulation of compressible turbulent flows', *J. Fluid Mech.*, **238**, 155–185 (1992).
7. B. Vreman, 'Direct and large eddy simulation of the compressible turbulent mixing layer', *Thèse*, Université de Twente, 1995.
8. B. Vreman, B. Geurts and H. Kuertell, 'Large eddy simulation of the turbulent mixing layer', *J. Fluid Mech.*, **339**, 357–390 (1997).
9. G.N. Coleman, J. Kim and R.D. Moser, 'A numerical study of turbulent supersonic isothermal-wall channel flow', *J. Fluid Mech.*, **305**, 159–183 (1995).
10. J.W. Deardorff, 'A numerical study of three-dimensional turbulent channel flow at large Reynolds number', *J. Fluid Mech.*, **41**, 453–480 (1970).
11. U. Schumann, 'Subgrid scale model for finite-difference simulations of turbulent flows in plane channels and annuli', *J. Comput. Phys.*, **18**, 376–404 (1975).
12. P. Moin and J. Kim, 'Numerical investigation of turbulent channel flow', *J. Fluid Mech.*, **118**, 341–377 (1982).
13. A.G. Kravchenko and P. Moin, 'On the effect of numerical errors in large eddy simulations of turbulent flows', *J. Comput. Phys.*, **131**, 310–322 (1997).
14. U. Piomelli, 'High Reynolds number calculations using the dynamic subgrid-stress model', *Phys. Fluids A*, **5**, 1484–1490 (1993).
15. J.P. Ridder and R. Beddini, 'Large eddy simulation of compressible channel flow', *NASA Tech. Report*, Grant NGT-50363, 1993.
16. W.P. Wang, 'On the large eddy simulation of turbulent channel flow with significant heat transfer', *Phys. Fluids*, **8**, 3354–3366 (1996).
17. S. Ghosal, 'An analysis of numerical errors in large eddy simulations of turbulence', *J. Comput. Phys.*, **125**, 187–206 (1996).
18. G.A. Blaisdell, E.T. Spyropoulos and J.H. Qin, 'The effect of the formulation of non-linear terms aliasing errors on spectral methods', *Appl. Numer. Math.*, **21**, 207–219 (1996).
19. P. Moin, K. Squires, W. Cabot and S. Lee, 'A dynamic subgrid-scale model for compressible turbulence and scalar transport', *Phys. Fluids A*, **3**, 2746–2757 (1991).
20. A. Favre, 'Equations stastistiques aux fluctuations turbulentes dans les écoulements compressibles: cas des vitesses et des températures', *C.R. Acad. Sci. Paris*, **273**, 1087 (1971).
21. A.W. Vreman, N.D. Sandham and K.H. Luo, 'Compressible mixing layer growth rate and turbulence characteristics', *J. Fluid Mech.*, **320**, 235–258 (1996).
22. P.S. Lowery and W.C. Reynolds, 'Numerical simulation of a spatially-developing, forced, plane mixing layer', *Report of the Stanford University*, *TF26*, 1986.
23. V. Deschamps, 'Simulation numérique de la turbulence inhomogène incompressible dans un écoulement de canal plan', *Note Technique ONERA*, 1988.
24. H.W. Liepmann and A. Roshko, 'Elements of gas dynamics', *Galcit Aeronautical Series*, Wiley, New York, 1957.
25. B. Vreman, B. Geurts and H. Kuertell, '*A priori* tests of large eddy simulation of compressible plane mixing layer', *J. Eng. Math.*, **29**, 299–327 (1995).
26. L. Ta Phuoc, 'Modèle de sous-maille appliqués aux écoulements instationnaires décollés', *DGA/DRET*, *Journée thématique DRET: aérodynamique instationnaire turbulente—aspects numériques et expérimentaux*, 1994.
27. J. Bardina, J.H. Ferziger and W.C. Reynolds, 'Improved turbulence models based on large eddy simulation of homogeneous, incompressible, turbulent flows', *Report TF-19*, Thermosciences Division, Department of Mechanical Engineering, Stanford University, 1983.
28. J. Bardina, J.H. Ferziger and W.C. Reynolds, 'Improved subgrid scale models for large eddy simulation', *AIAA Paper*, *80-1357*, 1980.
29. E. David, 'Modélisation des écoulements compressibles et hypersoniques: une approche instationnaire', *Doctorat*, Institut National Polytechnique de Grenoble, 1993.
30. P. Sagaut and B. Troff, 'Subgrid-scale model improvements for non-homogeneous flows', *First AFOSR International Conference on DNS and LES*, Ruston, USA, 4–8 August 1997.
31. P. Sagaut and R. Grohens, 'Discrete filters for large eddy simulation', *Int. J. Numer. Methods Fluids*, to appear.
32. S. Ghosal, T.S. Lund, P. Moin and K. Akselvoll, 'A dynamic localization model for large eddy simulation of turbulent flows', *J. Fluid Mech.*, **286**, 229–255 (1995).
33. K. Horiuti, 'Large eddy simulation of turbulent channel flow by one-equation modeling', *J. Phys. Soc. Jpn.*, **54**, 2855–2865 (1985).

34. M.A. Niederschulte, R.J. Adrian and T.J. Hanratty, 'Measurements of turbulent flow in a channel at low Reynolds numbers', *Exp. Fluids*, **9**, 222–230 (1990).
35. P.G. Huang, G.N. Coleman and P. Bradshaw, 'Compressible turbulent channel flows: DNS results and modeling', *J. Fluid Mech.*, **305**, 185–218 (1995).
36. J.A. Clark and E. Markland, 'Vortex structures in turbulent boundary layer', *Aeronaut. J.*, **74**, 243–244 (1970).
37. H.P. Kreplin and H. Eckelmann, 'Behavior of the three fluctuating velocity components in the wall region of a turbulent channel flow', *Phys. Fluids*, **22**, 1233–1239 (1979).
38. J. Kim, P. Moin and R. Moser, 'Turbulence statistics in fully developed channel flow at low Reynolds number', *J. Fluid Mech.*, **177**, 133–166 (1987).
39. R.B Dean, 'Reynolds number dependence of skin friction and other bulk flow variables in two-dimensional rectangular duct flow', *Trans. ASME J. Fluids Eng.*, **100**, 215–223 (1978).
40. F.M. Najjar and D.K. Tafti, 'Study of discrete test filters and finite difference approximations for the dynamic subgrid-scale stress model', *Phys. Fluids*, **8**, 1076–1088 (1996).
41. W.W. Willmarth, 'Measurements of the fluctuating pressure at the wall beneath a tick turbulent boundary layer', *J. Fluid Mech.*, **21**, 107–109 (1965).
42. J.A. Elliot, 'Microscale pressure fluctuations measured within the low atmospheric boundary layer', *J. Fluid Mech.*, **53**, 351–383 (1972).
43. C.G. Speziale, G. Erlerbacher. T.A. Zang and M.Y. Hussaini, 'The subgrid scale modeling of compressible turbulence', *Phys. Fluids*, **31**, 940–942 (1988).

